Universal Journal of Carbon Research
https://ojs.wiserpub.com/index.php/UJCR/

Research Article

Graphene Oxide/Nanocrystalline Cellulose Composite: A Facile Phase Modulator

Irene J. Ng'etich[1], Elijah Mwangi[2], Moses A. Ollengo[2*]

[1]Dedan Kimathi University of Technology Nyeri, Kenya
[2]University of Nairobi, Kenya
E-mail: mosesollengo@gmail.com

Received: 5 December 2022; **Revised:** 26 April 2023; **Accepted:** 23 May 2023

Abstract: In the past few years, graphene and graphene-based materials have received enormous interest from the scientific community due to their extraordinary mechanical, electronic, optical and electrochemical properties. The success of graphene applications highly motivates the exploration of other applications such as in designing of antennas, phase modulation, as a frequency multiplier, design of graphene-based Field Effect Transistors, its use as an electrode in batteries and as a supercapacitor. In this paper, we present the Graphene Oxide/ Nanocrystalline cellulose (GO/NCC) composite material experimental phase modulation investigation. The modulator produced a $0.2\pi^c$ phase shift and the temporal profile obtained. The insertion loss at an ideal voltage of 2V and the extinction ratio was determined to be 15.17 dB at 25MHz and 12.22 dB respectively. The $0.2\pi^c$ phase shift demonstrated by GO/NCC implies that it can be used in phase shift keying, specifically, in Off-set quadrature phase-shift keying modulation where a phase change of not greater than $\frac{\pi}{2}$ radians at a time is required.

***Keywords*:** phase modulation; insertion loss; extinction ratio; modulation index; graphene oxide/nanocrystalline cellulose (GO/NCC)

1. Introduction

Phase modulation, an angle modulation technique, is the process of varying the phase of the carrier signal linearly with the message signal. This technique is very critical and has a wide range of applications in digital communication. Apart from it being widely used for transmitting radio waves and being an integral part of many digital transmission coding schemes that underlie a wide range of technologies like Wi-Fi, GSM and satellite television, phase modulation also finds application in photonic systems such as in Fiber-optic sensors and gyroscopes, integrated-optics sensors, or high-performance photonic integrated circuits [1]. Such a photonic system can be integrated as the core part of some specific applications like biosensors, 5G advanced optical communication devices, gyroscopes, or high-performance computation devices [1].

Others include in military electromagnetic warfare applications [2], in Polar and out-phasing transmitters [3] and improvement of ultrasonic imaging in aluminum plates [4] among various other applications.

In engineering, figures of merit are the key parameters that are often defined for particular materials or devices in order to determine their relative utility for an application [5]. This also enables a comparison to be done on the material or device that has been fabricated against those previously fabricated for the same application.

Copyright ©2023 Irene J. Ng'etich, et al.
DOI: https://doi.org/10.37256/ujcr.1120232216
This is an open-access article distributed under a CC BY license
(Creative Commons Attribution 4.0 International License)
https://creativecommons.org/licenses/by/4.0/

The key phase modulator parameters include: extinction ratio, insertion loss, modulation index and the modulation efficiency.

The Phase modulation index describes the peak phase difference between the modulated and unmodulated signal, given as h:

$$h = \Delta\boldsymbol{\theta} \quad \text{(i)}$$

The insertion loss (IL) defines the loss or gain that is apparent upon inserting the network or device to be measured between a given source and a given receiver [6, 7]. It is given by:

$$\text{Insertion Loss (IL)} = 10\mathbf{log_{10}}(\mathbf{P}_{\boldsymbol{in}}/\mathbf{P}_{\boldsymbol{out}}) \quad \text{(ii)}$$

where P_{in} is power incident to the modulator, and P_{out} is the power transmitted from the modulator.

On the other hand, the extinction ratio gives the ratio of optical power when a one is transmitted versus when a zero is transmitted [8], given by:

$$\text{Extinction Ratio (ER)} = \mathbf{P_1}/\mathbf{P_0} \quad \text{(iii)}$$

where P_1 is the optical power level generated when the light source is on, and P_0 is the power level generated when the light source is off.

These key parameters have been determined for the conventional phase modulators such as the Silicon-based phase modulators [9–12] and Lithium niobate ($LiNbO_3$) phase modulator [13,14] among others.

However, most of the above-mentioned modulators suffer from low modulation efficiency, large footprint, substantial temperature sensitivities, narrow operating bandwidth, and high insertion loss [15]. To be able to mitigate those limitations, a modulator with ultra-compact device footprint, small insertion loss, low energy consumption, ultrafast response, high modulation speed, broad operation bandwidth, and acceptable thermal tolerance is highly desirable [15].

Graphene [16] features unique properties such as strong coupling with light, gate-variable optical conductivity, extraordinary thermal conductivity in the range of 3000–5300W/mK [17], and ultrahigh saturable absorption [18], which show great potential applications in optical modulators.

A.Wirth-Lima et al. [19] presented Graphene-based Binary Phase-shift keying (BPSK) and Quadrature Phase Shift Keying (QPSK) modulators which could operate in the range from the Tera-Hertz up-to the infrared. These devices were noted to have huge advantages over the Silicon Mach-Zehnder optical modulators (MZMs) with lateral PN-junction rib-waveguide phase shifters such as having only one waveguide and a much simpler application system of the modulator signal (gate voltage) than in silicon MZMs. A series of theoretical investigations and experimental demonstrations of graphene-based modulators have been extensively researched [20–28].

Tables 1 and 2 show a summary of select modulators with their respective extinction ratio and insertion losses:

Table 1. Summary of the extinction ratio and insertion losses for select modulators

Material	Author	Insertion Loss (dB)	Extinction Ratio (dB)	Frequency (GHz)	Bias Voltage (V)
Silicon	M. Moradi et al.	−0.76	19.81	193 GHz	-
Graphene	A. Mohammed et al.	6.2	3.5	100 GHz	2.18
Lithium Niobate	C. Shang et al.	12	33	67 GHz	2
Silicon	J. Liu et al.	-	55	11 GHz	2
EAM	M. Connelly	30		10 GHz	2

Table 2. Review of select phase modulator types and their basic performance

Authors	Phase Modulator Type	Freq	Phase Change	Insertion Loss
H.T. Chen et al.	Metasurface with doped GaAs	880–900 GHz	32.4º	6 dB
T. Jiang et al.	Metasurface with doped Si	0.5–1.56 THz	52.2º	6 dB
S Y. Sun et al.	Metasurface with Liquid Crystal	80–120 GHz	349.2º	25 dB
Z. Chen et al.	Metasurface with Graphene	0.5–1.6 THz	140.4º	10 dB

In this paper, we present a Graphene Oxide/Nanocrystalline Cellulose (GO/NCC) Phase modulator that offers huge advantages as compared to the silicon based MZMs such as having a much simpler design, greater efficiency and is cheaper. The GO/NCC composite material also has several advantages when compared to other graphene-based materials such as flexibility and stretchability, as well as an increase in adsorption capacity, photo-thermal activity, stability, intrinsic luminescence and fluorescence, optical transparency, and thermal conductivity. The phase shift, temporal profile as well as the key figures of merit that include the modulation index, extinction ratio and insertion loss is experimentally determined.

2. Materials and methods

2.1 *Synthesis of Nanocrystalline Cellulose (NCC)*

The NCC was produced using dissolving pulp derived from a hard wood source. The process involved hydrolysis with 65% m/m sulfuric acid, wherein 5 g of dissolving pulp was mixed with 100 ml of the acid solution and stirred vigorously (700 PM) at 64 °C for 1 hour. To stop the hydrolysis reaction, the mixture was diluted 10-fold with deionized water, and the resulting mixture was centrifuged at 9000 RPM using a Hettich Zentrifugen, Universal 320 R centrifuge for 15 minutes. The centrifugation step helped to concentrate the cellulose and remove excess aqueous acid. The resulting solid material was rinsed with distilled water and centrifuged three times. Subsequently, the material was dialyzed against deionized water using Sigma-Aldrich dialysis sacks for one week until the pH of the solution reached 7. Finally, the dialyzed nanocellulose was sonicated in an ultrasonic bath for 5 minutes under cooling in a bath at 75% output and 0.7 cycles to obtain a NCC colloidal solution [29].

2.2 *Synthesis of Graphene Oxide*

The synthesis of Graphene Oxide (GO) was achieved using a modified Hummer's method [29]. Initially, Graphite was combined with Sulphuric acid in a reaction vessel. Sodium Nitrate was added to the mixture while keeping it in an ice water bath, and Potassium permanganate (KMn04) was subsequently introduced. The reaction was carried out at a temperature below 15 °C, resulting in the formation of Graphene Oxide. The reaction temperature was then raised to 50 °C, and Hydrogen Peroxide was added to the mixture. The resulting GO was washed several times with double deionized water (Dl) until the pH of the filtrate was neutral. To determine the concentration of the synthesized GO, duplicate aliquots were accurately weighed, and the aliquots were then dried overnight in an oven set at 50 °C. The dried aliquots were reweighed, and the concentration was calculated as the average mass of the duplicate aliquots after drying over the average mass before drying [29].

2.3 *Synthesis of Graphene Oxide/Nanocrystalline Cellulose (GO/NCC)*

The NCC/GO composite was then prepared by dispersing the Graphene Oxide synthesized in an ultrasonic water bath treatment as the NCC was added. The resultant composite solution was transferred to a petri-dish to allow for slow evaporation of water in a controlled dust-free environment and dried in order to obtain the composite film. Composites having 1%, 5%, 10%,15%, 20%,25%, 30%, 35%, 40% and 50% concentration of NCC per mass of the GO/NCC were obtained [29].

2.4 *Characterization of the Graphene Oxide/Nanocrystalline Composite Material*

2.4.1 *Reflectance Measurement*

The PerkinElmer lambda 35 double beam UV-vis spectrometer, equipped with a Labsphere RSA-PE-20 integrating sphere, was used to obtain the UV-visible-NIR spectra of the films [29].

2.4.2 *Hall Effect Measurements*

A typical Hall probe and four-probe approach without a magnetic field was used to test the conductivity and anomalous Hall effect at ambient temperature. Using a digital multimeter and an electrometer respectively, the current and the Hall voltage were measured [29].

2.4.3 *Atomic Force Microscopy*

The NT-MDT Solver P47H base was used for Atomic Force Microscopy (AFM). The preferred cantilever had a resonance frequency of 146–236 kHz, a force constant of 21–98 N/m, a typical tip radius of 2 nm, and a scan rate that ranged from 0.6–1.6 Hz. Before analysis, thin films with varying NCC/GO compositions were mounted to a glass slide using dual adhesive tape. Film thickness for the GO/NCC composite with was estimated using the AFM, 2D scale [29].

2.4.4 *3D Optical Microscopy*

The GO/NCC composite material was mounted on a slide and placed in the scanning electron and the Zeiss Axio zoom camera microscopes to obtain the 3D images of the film.

2.4.5 *Modulation Index/Temporal Profile*

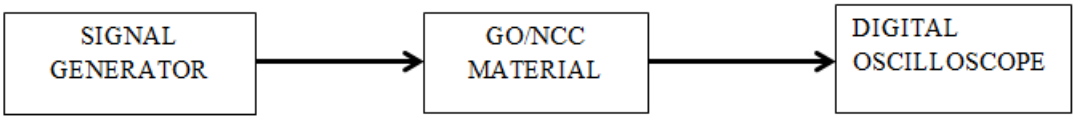

Figure 1. Block diagram set-up for the determination of the temporal profile and phase shift effected by the GO/NCC Modulator material

The temporal profile and phase shift effected by the GO/NCC composite material was determined by connecting the signal generator to the GO/NCC which was held firmly in place by two wooden holders and two copper plates, that were overlaid on the GO/NCC material, which served as the contacts that enabled the anchoring of the probes (as shown in figure 2).

Figure 2. Copper plates overlaid on the GO/NCC composite material

The output of the modulator material was connected to the Digital oscilloscope using scope probes in order to obtain the temporal profile and consequently, the phase shift. The phase difference was obtained using the formula:

$$\text{Phase difference, } \Delta\boldsymbol{\theta} = 360 \times f \times \Delta t \qquad \text{(iv)}$$

where f is the operational frequency and Δt the time difference between the modulated and unmodulated signal.

2.4.6 *Insertion loss*

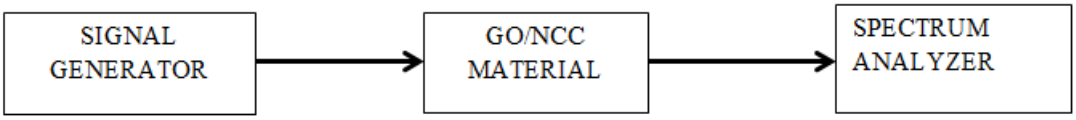

Figure 3. Block diagram set-up for the determination of the insertion loss

To determine the Insertion Loss, the RF Signal generator was connected to the Graphene Oxide/Nanocrystalline Cellulose phase modulator and the output connected to the spectrum analyzer. The power input (P_{in}) and power output from the modulator (P_{out}) was obtained from the spectrum analyzer as the voltage and frequency were varied from 0 to 20Vand 0 to 25MHz respectively whereby the 20V and 25MHz were the highest voltage and frequency that could be attained using the signal generator used in the experiment.

The insertion loss was determined using the formula:

$$\text{Insertion Loss, } I_L = 10 \log_{10}\left(\frac{P_{in}}{P_{out}}\right) \quad \text{(v)}$$

where P_{in} is the power incident to the modulator material & P_{out} is the power transmitted from the modulator material.

2.4.7 *Extinction Ratio*

The extinction ratio was determined by connecting the GO/NCC modulator material to the Optical source of the Scientech Optical communication system having a 660 nm wavelength and the output power, when the optical source was switched on and off, was obtained from the network analyzer.

$$\text{Extinction Ratio (ER)} = \mathbf{P_1/P_0} \quad \text{(vi)}$$

where P_1 is the optical power level generated when the light source was on, and P_0 is the power level generated when the light source was off.

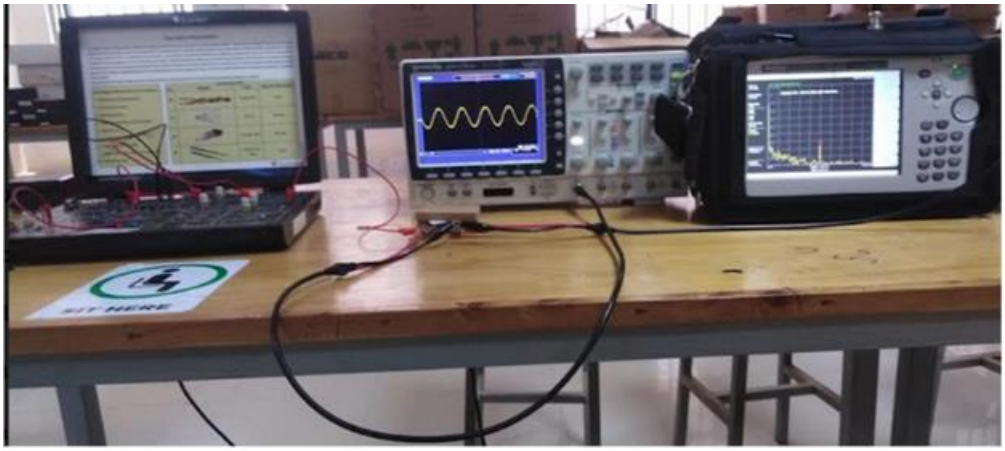

Figure 4. Set-up for the determination of the extinction ratio

3. Results and Discussion

In comparison to graphene, Graphene Oxide displays a markedly altered charge hopping parameter in the band gap. The electronic density of states (DOS) and the electronic wave functions of localized states are related to the hopping. It was anticipated that the addition of an NCC insulating layer to the surface of GO would promote localized states away from the Fermi energy level (E_F) rather than favor delocalization of carriers. The localized disorders in NCC/GO composites improved the mid-gap energy states. A distinct change in the UV-vis-NIR spectra of the composites at the different NCC composition was detected as a result; this is shown in Figure 5 [29].

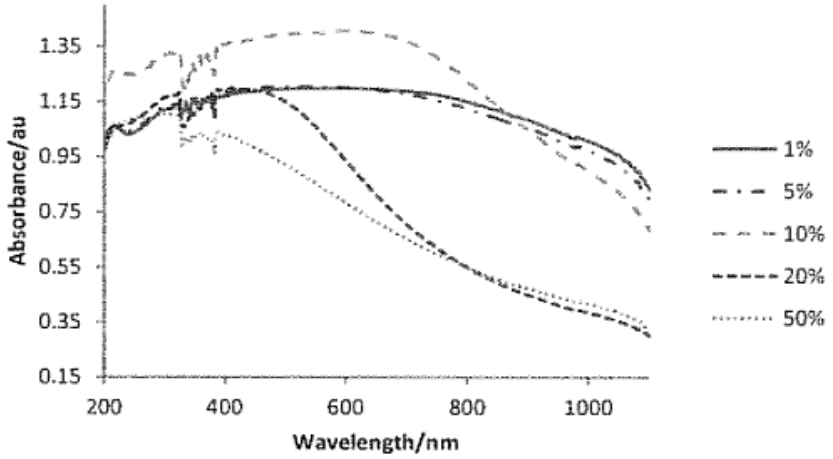

Figure 5. UV-vis-IR response of the thin films [29]

With a considerably higher absorption in the visible/NIR range, these spectra reveal a noticeable induction of band gap features at a 10 mass% NCC composition. It can therefore be true that rising intra- and interfacial displacements are a direct outcome of the higher mass% NCC integration. The strength of the interference with the intermolecular electronic couplings caused by these torsional effects depends on the bonding-antibonding characteristics of the border molecular orbitals, which include the highest occupied molecular orbital (HOMO) and the lowest unoccupied molecular orbital (LUMO) [29].

The distribution of electronic couplings in the composite layers results in conducting paths across the thin film acting as dead-ends for the charges because of differences in the amount of interactions between nearby molecules or chain segments with reference to their relative locations and alignments, known as off-diagonal disorder, this is clearly shown in figure 6.

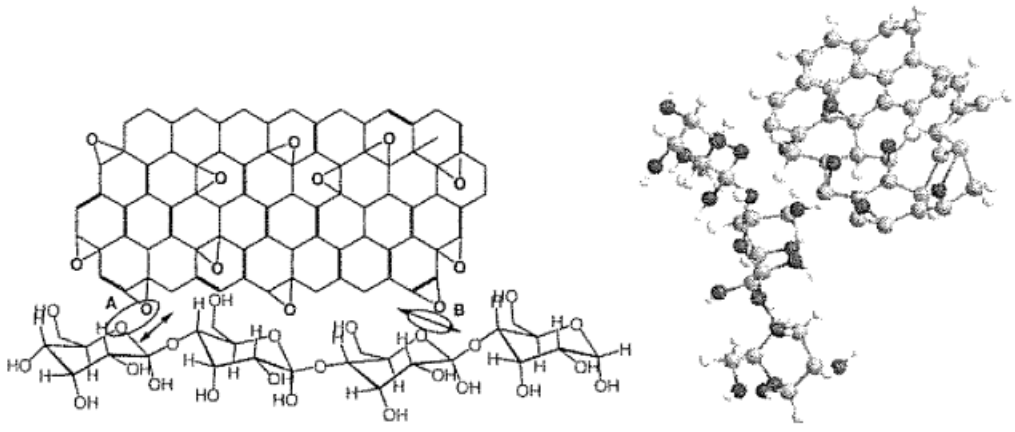

Figure 6. A and B in a GO/NCC composite representing the diagonal and off-diagonal disorders, respectively, caused by the epoxy oxygen on GO and the oxygen in the NCC [29]

The presence of oxygen and hydrogen atoms in the GO layer results in diagonal disorder by producing pseudo-finite-size conjugated segments with varying lengths and, consequently, differing HOMO and LUMO energies. These diagonal disorders are caused by electrostatic effects from nearby molecules, which change depending on local packing variations. It may be inferred that the heteroatoms in the GO monolayer act as mini dipoles and polarizing centers. Similar to this, the cellulose has tiny dipole centers arranged in predictable repeating units. So, in such composites, it is expected that the degree/extent of both disorders will grow in a concentration-dependent manner [29].

In figure 5, that shows the UV-visible-NIR spectra of variable mass %NCC in NCC/GO composite thin films, instead of π - π * transitions, which generally exhibit an absorption band between 225 and 275 nm, the optical

absorption of the NCC/GO composite is characterized by η- π* transitions. This suggests a different combination of charge carriers, perhaps as a result of competing electron-electron and electron-phonon interaction. The amount of NCC integrated into the GO matrix was found to affect these coupling effects. Whereas 10 mass %, 20 mass%, and 50 mass% NCC have shoulders at 655, 445, and 393 nm, respectively, 1 mass% NCC and 5 mass% NCC com positions do not. This suggests that conduction electrons with photon energies in the visible/near-UV region contribute significantly, albeit their contribution declines as NCC mass percentage increases. The characteristic GO absorption spectra has a shoulder at approximately 300 nm (η- π *) that is typically attributed to C-O transitions and a maximum around 230 nm (π - π *). However, these composites did not exhibit these characteristics. No discernible bandgap could be seen at any of the compositions under consideration indicated by lack of a visible absorption edge. The lone pairs on the oxygen are the sole participating electrons. As a result, the amount of NCC incorporated into the GO films relates directly with the composite's band gap energy [29].

Different topological surface morphology was seen in the 2D atomic force microscopy images as shown in figure 7 for NCC/GO composites with various mass percent compositions.

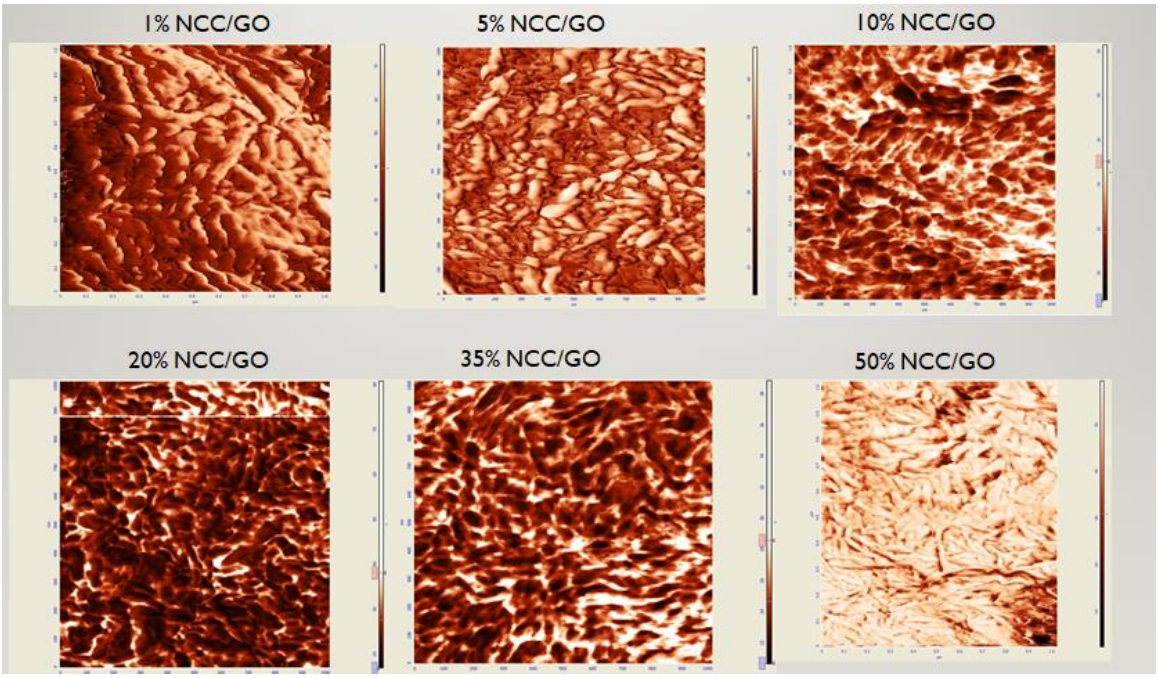

Figure 7. Atomic microscopy images at 1 mass %, 5 mass %, 10 mass %, 20 mass %, 35 mass % and 50 mass % GO/NCC

The 1 mass% NCC/GO composite, in particular, displayed spiky topography that gradually smoothed out at 5 mass% and eventually attained some alignment at 20 mass% NCC/GO composite. At 50% mass% NCC/GO composite, there is significant wrinkling that interferes with the alignment. Spiky edges are also present.

The composite made of 20 mass% NCC and GO reveals honeycomb patterns that resemble graphene sheets. The development of these structures shows that there was a clear electronic interaction between the oxygen-carrying groups on the GO fabric and the OH groups on the NCC. High electron density and regular pentagonal and heptagonal honeycomb patterns define the sp2 rich graphene sheet. The minimal deformation of the structures at 20 mass% NCC/GO composition indicates that no sp2 hybridized carbons have been reformed, only a surface reorganization of the NCC to create interconnecting channels. The composite could exhibit n-type organic semiconductor properties as a result of the injection of electrons into its conductive band through the use of the constructed channels [29].

It is possible to identify the main charge carriers and innate mobility in such materials by measuring the Hall effects. Hoping carriers typically travel in the opposite direction as the Lorentz force operating on the charge carriers due to the effect of a transverse Hall electric field. The predominant charge carrier determines the polarity of the measured Hall voltage. A positive Hall voltage implies that the "holes" are the predominant charge carriers, while a negative sign denotes electrons as the predominant charge carrier [29].

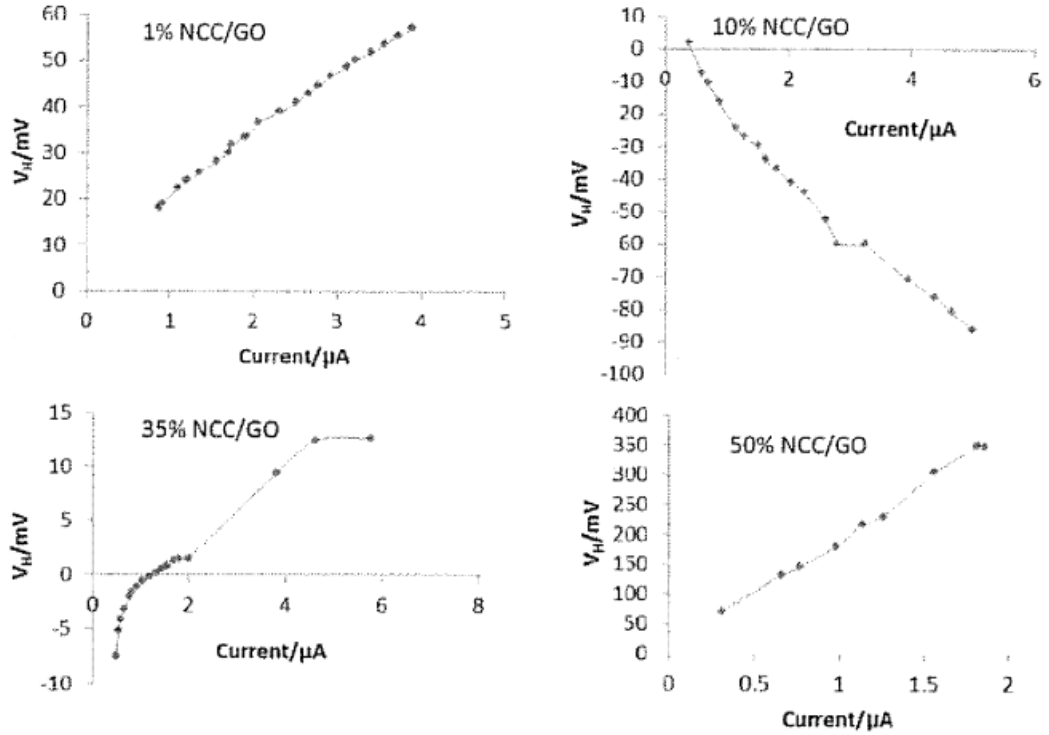

Figure 8. The relationship between Hall voltage and input current at variable compositions of NCC in graphene oxide [29]

Referring to figure 8, a positive slope represents the “hole” dominated transport while a negative slope depicts the “electron” dominated transport. The major charge carriers in the 1, 5, and 50 mass% NCC/GO composites were "hole" conduction (p-type), while the dominant charge carriers in the 10 and 20 mass% NCC/GO composites were "electron" conduction (n-type). At high currents, the 35 mass% NCC/GO composite displayed a p-type transition. It may be linked to the enlarged electronic band of states' thermal degradation caused by current flow. Hence, it has been shown that it is possible to create unipolar (solely n- or p-type) materials or generate well-patterned p- and n-type regions on the same film by altering the concentration of NCC in an NCC/GO composite. Novel charge carrier characteristics and thus distinct topological electrical conductivity features are produced by the variation in the composite composition. The long-range conductivity that is exhibited in the composite films and the composition-dependent properties of charge switch carriers that have been clearly shown is a potent feature in radio frequency phase charge that is useful for phase modulation [29].

An energy extraction behavioral profile for the different NCC compositions using 9mW and 4.06mW lasers was obtained as shown in figure 9.

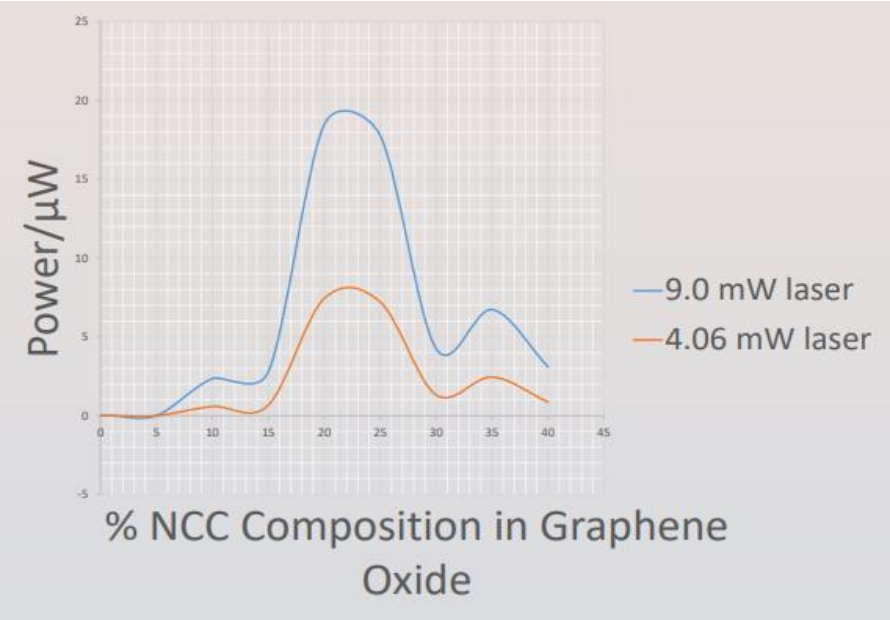

Figure 9. Energy extraction behavior at various NCC compositions [29]

The peak energy extraction was observed in the range of 20–25 mass % of NCC in the NCC/GO composite. The 25 mass% NCC was chosen for further phase modulation characterization of the GO/NCC material.

A 3D image of the Graphene Oxide/Nanocrystalline Cellulose sample synthesized was obtained by using the Zeiss Axio Zoom.V16 Camera Microscope, which measures in the micrometer range and showed the surface morphology of the GO/NCC, having a magnification of 260× and the Scanning Electron Microscope (SEM) that measured in the nanometer range. The rod-like structures had a measured peak height of 10nm. These rod-like or whisker-shaped structures form the characteristic identification of the Nanocrystalline cellulose present in the composite material having 25 mass % NCC of the GO/NCC. The Nanocellulose was obtained from cellulose which is a semi-crystalline polysaccharide [$(C_6H_{12}O_5)_n$] consisting of D-glucopyranose units joined by β-(1-4)-glycosidic linkages. The application of acid treatment eliminates the majority of the non-crystalline cellulose, resulting in the production of cellulose crystals with high purity. As a result, the NCC possesses a high degree of crystallinity. The interflake separation distance differed for the different NCC compositions as summarized in table 3.

Table 3. Interflake separation distance

FLAKE TYPE	INTERFLAKE SEPARATION/nm
5% NCC	11.12 ± 2.77
10% NCC	5.91 ± 1.72
15% NCC	5.74 ± 2.11
20% NCC	6.58 ± 1.65
25% NCC	5.30 ± 1.43
AVERAGE	**7.34 ± 2.55**

The material was not subjected to any special conditions to control its growth thickness.

When a signal from the signal generator was passed through the sample, measuring 6cm by 3cm in length and width respectively, a phase shift $0.2\pi^c$ was realized. The temporal profile was obtained from the Cathode Ray Oscilloscope and plotted as shown in Figure 12.

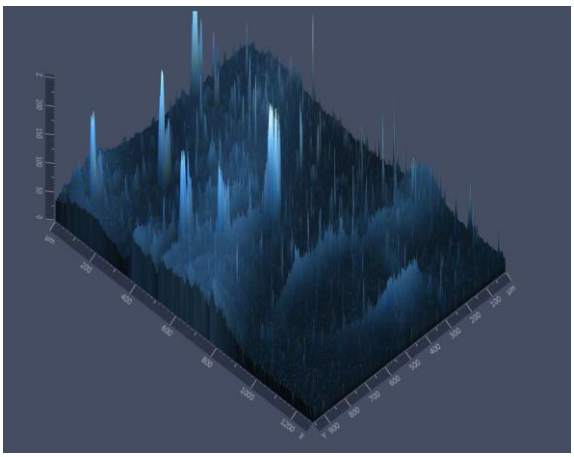

Figure 10. 3D image of the GO/NCC sample film synthesized having a thickness of 49.41µm with projections as observed under the Zeiss Axio Zoom.V16 Camera Microscope

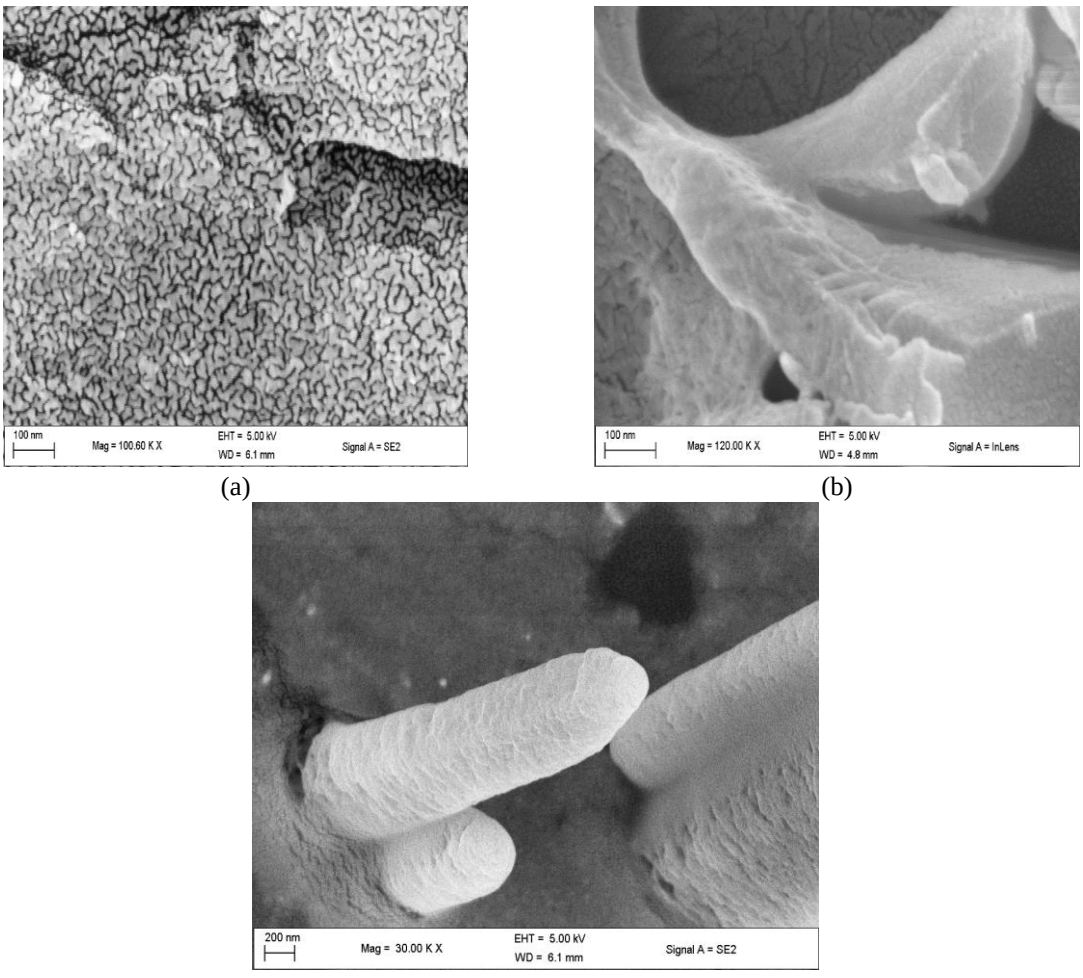

(a) (b)

(c)

Figure 11. SEM IMAGE of (a) GO and (b) NCC and (c) GO/NCC

The high number of OH groups on the surface of nanocrystalline cellulose is likely to favor hydrogen bonding. In this regard, the hydrogen bonding becomes the binding force between a nanocrystalline cellulose film sandwiched between two graphene oxide sheets, thereby forming a composite film. The nanocrystalline cellulose forms a thin layer of rods as shown in figure 11(c) in between the graphene oxide monolayers since it assumes nematic order, having no positional order but tend to point in the same direction (global orientation order), in colloidal dispersions occasioned by whisker entanglements. The interaction between the chiral surfaces and the twisted morphology of nanocrystalline cellulose and the overlaying graphene oxide monolayer provides an avenue for response to external applied electric or magnetic fields.

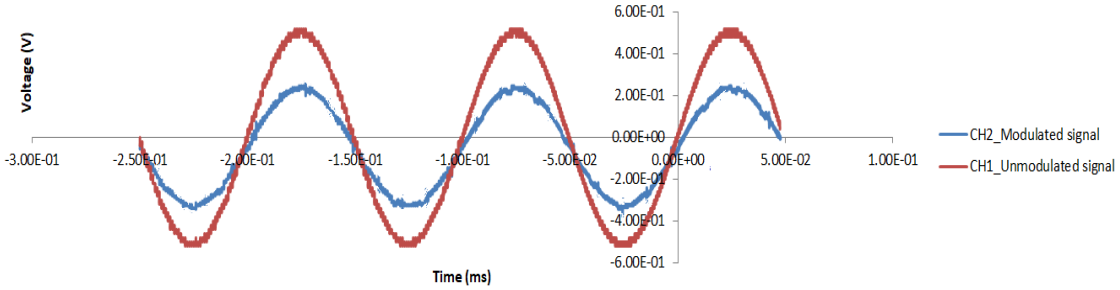

Figure 12. Temporal Profile of the GO/NCC modulator exhibiting the phase shift

The insertion loss experiment was performed on the GO/NCC as the voltage was varied from 0V to 20V and the graph obtained is as shown in Figure 13(a). A clearer profile of the graph obtained from the insertion loss experiment is as shown in Figure 13(b) as the voltage was varied from 2V to 20V.

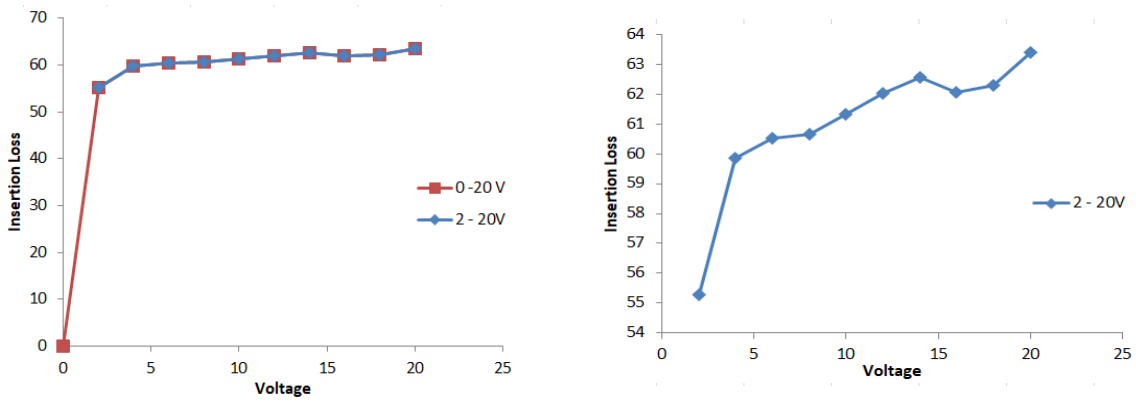

(a) (b)

Figure 13 GO/NCC modulator Insertion loss with increasing voltage: (a) 0V–20V and (b) 2V–20V

The Graphene Oxide structure consists of the sp^2 carbons that have a higher electronegativity value of carbon, while the sp^3 carbons, by virtue of them being hooked to oxygen, are devoid of electrons. Hence, they act as holes. Oxygen is more electro-negative than carbon, therefore, carbon will appear positive. This essentially creates a hole within the structure of Graphene Oxide.

The NCC held in between the Graphene Oxide is presumed to be a perfect insulator. However, due to the presence of oxygen groups, it can easily promote coupling. This therefore explains the phenomenon that is observed between 0 to 2 V, as shown in Figure 13(a), where there is an upsurge of the energy consumed due to a higher combination, that is, the electron-electron and electron-phonon coupling.

From 2V onwards to 20V, there is a gradual increase in energy consumed since it is now majorly driven by the electron – phonon couplings. As a higher voltage is applied, variations are observed that is attributed to the changes in the structure of the GO/NCC.

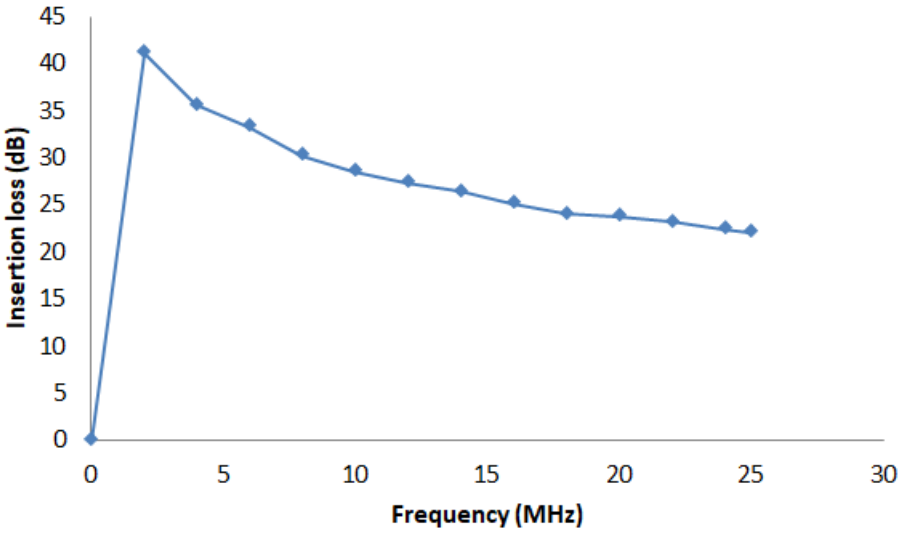

Figure 24. GO/NCC Insertion loss vs frequency

Figure 14 shows the graph of the GO/NCC insertion loss with increasing frequency. Initially, the insertion loss increased before significantly decreasing upon increase of frequency. This confirms the work done by W. Kim et al. on radio frequency characteristics of graphene oxide where the impedance and resistance of graphene sheets drastically decrease as frequency increases. Consequently, the insertion loss also decreases. This confirms graphene oxide has a high potential for use at gigahertz ranges.

Normally, a driving voltage of above 5V is not compatible with the microelectronic integrated circuits since it is very difficult for CMOS chips to supply such a high voltage at a high frequency. Also, a higher voltage (above 5V) results in the widening of the noise margin and this is undesirable. Low voltage also means low power consumption and less heat dissipation problems. Therefore, at an ideal voltage of 2V, an insertion loss of 15.17dB at 25MHz was obtained.

An extinction ratio (ER) of 12.22dB was obtained for the GO/NCC modulator. The ER is an important metric since it has an impact on a device's performance. It should be ideally larger than 10dB. As the extinction ratio improves, the Bit-error ratio improves, reducing the number of errors and the amount of error correction required. A poorer value of ER increases the power penalty and worsens the Bit Error Ratio.

4. Conclusions

In conclusion, the GO/NCC Phase Modulator has been characterized using the following key parameters: The modulator produced a 0.2π radians phase shift and the temporal profile obtained. The $0.2\pi^{c}$ modulation index demonstrated by GO/NCC implies that it can be used in phase shift keying, specifically, in Off-set quadrature phase-shift keying modulation where a phase change of not greater than $\frac{\pi}{2}$ radians at a time is required. The insertion loss at an ideal voltage of 2V and the extinction ratio was determined to be 15.17 dB at 25MHz and 12.22dB respectively. Ideally, the insertion loss and the extinction ratio should generally be lower than a few dB and larger than 10dB respectively for a modulator.

Further study can be done on this novel material to improve on its key parameters such as further lowering the insertion loss to nearly 0dB. Reduced Graphene Oxide may be used instead, the operational frequency increased and the effect of these changes on the modulation index, insertion loss and extinction ratio investigated. The remaining key figures of merit, that is, the power consumption and modulation efficiency for this particular material may also be determined.

Conflict of interest

There is no conflict of interest for this study.

References

1. R. Menéndez, "Modulation in Electronics and Telecommunications - Optical Phase-Modulation Techniques," vol. 10.5772/intechopen.75319, 2019, doi: 10.5772/intechopen.90343.
2. Urick, V.J.; Bucholtz, F.; Devgan, P.S.; McKinney, J.D. Analog Phase Modulation for Avionics Applications. **2007**, 7–8, https://doi.org/10.1109/avfop.2007.4365721.
3. Nidhi, N.; Su, P.-E.; Pamarti, S. Open-Loop Wide-Bandwidth Phase Modulation Techniques. *J. Electr. Comput. Eng.* **2011**, *2011*, 1–12, https://doi.org/10.1155/2011/507381.
4. Tischer, R.M.; Higuti, R.T.; Prado, V.T.; Kitano, C. Improving ultrasonic imaging of aluminum plates using phase modulation. *J. Integr. Circuits Syst.* **2020**, *15*, 1–5, https://doi.org/10.29292/jics.v15i3.191.
5. Olivieri, A.C.; Escandar, G.M. Analytical Figures of Merit. **2014**, 93–107, https://doi.org/10.1016/b978-0-12-410408-2.00006-5.
6. W. Valkenburg, "Reference Data for Engineers - Radio, Electronics, Computer, etc, 9 ed. Newnes", 2002.
7. Ams, M.; Little, D.; Withford, M. Femtosecond-laser-induced refractive index modifications for photonic device processing. **2012**, 305–332, https://doi.org/10.1533/9780857096227.3.305.
8. C. DeCusatis, "Handbook of Fiber Optic Data Communication 4ed." Elsevier, 2014.
9. Mahrous, H.; Azmy, M.; Afifi, A.; AbouElainain, A.; Kotb, A.; Fedawy, M.; Fikry, W.; Gad, M.; Selim, D. Design of compact, high-speed and low-loss silicon-on-silica electro-optic modulators. *Semicond. Sci. Technol.* **2020**, *35*, 095017, https://doi.org/10.1088/1361-6641/ab9d09.
10. Kieninger, C.; Füllner, C.; Zwickel, H.; Kutuvantavida, Y.; Kemal, J.N.; Eschenbaum, C.; Elder, D.L.; Dalton, L.R.; Freude, W.; Randel, S.; et al. Silicon-organic hybrid (SOH) Mach-Zehnder modulators for 100 GBd PAM4 signaling with sub-1 dB phase-shifter loss. *Opt. Express* **2020**, *28*, 24693, https://doi.org/10.1364/oe.390315.
11. Zhao, X.; Shah, U.; Glubokov, O.; Oberhammer, J. Micromachined Subterahertz Waveguide-Integrated Phase Shifter Utilizing Supermode Propagation. *IEEE Trans. Microw. Theory Tech.* **2021**, *69*, 3219–3227, https://doi.org/10.1109/tmtt.2021.3076079.
12. Zhang, Y.; Gao, J.; Qin, S.; Cheng, M.; Wang, K.; Kai, L.; Sun, J. Asymmetric Ge/SiGe coupled quantum well modulators. *Nanophotonics* **2021**, *10*, 1765–1773, https://doi.org/10.1515/nanoph-2021-0007.
13. Kharel, P.; Reimer, C.; Luke, K.; He, L.; Zhang, M. Breaking voltage–bandwidth limits in integrated lithium niobate modulators using micro-structured electrodes. *Optica* **2021**, *8*, 357, https://doi.org/10.1364/optica.416155.
14. Choudhary, K.; Singh, A.; Singh, A.; Chaudhary, D.; Kumar, S. Implementation of highly optimized optical all logic gates on a single chip using Ti-diffused lithium-niobate for high-speed processing in combinational circuits. *Microelectron. J.* **2021**, *111*, 105048, https://doi.org/10.1016/j.mejo.2021.105048.
15. Hu, X.; Wang, J. Design of graphene-based polarization-insensitive optical modulator. *Nanophotonics* **2018**, *7*, 651–658, https://doi.org/10.1515/nanoph-2017-0088.
16. Geim, A.K.; Novoselov, K.S. The rise of graphene. *Nat. Mater.* **2007**, *6*, 183–191, doi:10.1038/nmat1849.
17. Mbambo, M.C.; Khamlich, S.; Khamliche, T.; Moodley, M.K.; Kaviyarasu, K.; Madiba, I.G.; Madito, M.J.; Khenfouch, M.; Kennedy, J.; Henini, M.; et al. Remarkable thermal conductivity enhancement in Ag—decorated graphene nanocomposites based nanofluid by laser liquid solid interaction in ethylene glycol. *Sci. Rep.* **2020**, *10*, 1–14, https://doi.org/10.1038/s41598-020-67418-3.
18. Qi, Y.-L.; Liu, H.; Cui, H.; Huang, Y.-Q.; Ning, Q.-Y.; Liu, M.; Luo, Z.-C.; Luo, A.-P.; Xu, W.-C. Graphene-deposited microfiber photonic device for ultrahigh-repetition rate pulse generation in a fiber laser. *Opt. Express* **2015**, *23*, 17720–6, https://doi.org/10.1364/oe.23.017720.
19. Wirth-Lima, A.J.; Bezerra-Fraga, W. Graphene-based BPSK and QPSK modulators working at a very high bit rate (up Tbps range). *Opt. Quantum Electron.* **2021**, *53*, 1–16, https://doi.org/10.1007/s11082-021-02928-6.
20. Lu, Z.; Zhao, W. Nanoscale electro-optic modulators based on graphene-slot waveguides. *J. Opt. Soc. Am. B* **2012**, *29*, 1490–1496, https://doi.org/10.1364/josab.29.001490.
21. Yang, L.; Hu, T.; Hao, R.; Qiu, C.; Xu, C.; Yu, H.; Xu, Y.; Jiang, X.; Li, Y.; Yang, J. Low-chirp high-extinction-ratio modulator based on graphene–silicon waveguide. *Opt. Lett.* **2013**, *38*, 2512–2515, https://doi.org/10.1364/ol.38.002512.
22. Koester, S.J.; Li, M. High-speed waveguide-coupled graphene-on-graphene optical modulators. *Appl. Phys. Lett.* **2012**, *100*, 171107, https://doi.org/10.1063/1.4704663.
23. Gosciniak, J.; Tan, D.T.H. Theoretical investigation of graphene-based photonic modulators. *Sci. Rep.* **2013**, *3*, srep01897, https://doi.org/10.1038/srep01897.

24. Xu, C.; Jin, Y.; Yang, L.; Yang, J.; Jiang, X. Characteristics of electro-refractive modulating based on Graphene-Oxide-Silicon waveguide. *Opt. Express* **2012**, *20*, 22398–22405, https://doi.org/10.1364/oe.20.022398.
25. Sensale-Rodriguez, B.; Yan, R.; Zhu, M.; Jena, D.; Liu, L.; Xing, H.G. Efficient terahertz electro-absorption modulation employing graphene plasmonic structures. *Appl. Phys. Lett.* **2012**, *101*, 261115, https://doi.org/10.1063/1.4773374.
26. Sensale-Rodriguez, B.; Yan, R.; Kelly, M.M.; Fang, T.; Tahy, K.; Hwang, W.S.; Jena, D.; Liu, L.; Xing, H.G. Broadband graphene terahertz modulators enabled by intraband transitions. *Nat. Commun.* **2012**, *3*, 780, https://doi.org/10.1038/ncomms1787.
27. Phare, C.T.; Lee, Y.-H.D.; Cardenas, J.; Lipson, M. Graphene electro-optic modulator with 30 GHz bandwidth. *Nat. Photonics* **2015**, *9*, 511–514, https://doi.org/10.1038/nphoton.2015.122.
28. Dalir, H.; Xia, Y.; Wang, Y.; Zhang, X. Athermal Broadband Graphene Optical Modulator with 35 GHz Speed. *ACS Photon*- **2016**, *3*, 1564–1568, https://doi.org/10.1021/acsphotonics.6b00398.
29. B. Martincigh, V. Nyamori, M. Ollengo, E. Mombeshora, and V. Moodley, "Nanocrystalline cellulose/graphene oxide composite versatile material for optoelectronic, photonic, and spintronic application," WO 2018/167634 Al- 2018, doi: WO2018167634.